

Large nonadiabatic quantum molecular dynamics simulations on parallel computers

Fuyuki Shimojo^{a,b,c,d}, Satoshi Ohmura^{a,b,c,d,e}, Weiwei Mou^{a,b,c}, Rajiv K. Kalia^{a,b,c}, Aiichiro Nakano^{a,b,c,*}, Priya Vashishta^{a,b,c}

^a Collaboratory for Advanced Computing and Simulations, Department of Physics & Astronomy, University of Southern California, Los Angeles, CA 90089-0242, USA

^b Department of Computer Science, University of Southern California, Los Angeles, CA 90089-0242, USA

^c Department of Chemical Engineering & Materials Science, University of Southern California, Los Angeles, CA 90089-0242, USA

^d Department of Physics, Kumamoto University, Kumamoto 860-8555, Japan

^e Department of Physics, Kyoto University, Kyoto 606-8502, Japan

ARTICLE INFO

Article history:

Received 9 July 2012

Received in revised form

18 July 2012

Accepted 9 August 2012

Available online 14 August 2012

Keywords:

Nonadiabatic quantum molecular dynamics

Time-dependent density functional theory

Surface hopping

Parallel computing

ABSTRACT

We have implemented a quantum molecular dynamics simulation incorporating nonadiabatic electronic transitions on massively parallel computers to study photoexcitation dynamics of electrons and ions. The nonadiabatic quantum molecular dynamics (NAQMD) simulation is based on Casida's linear response time-dependent density functional theory to describe electronic excited states and Tully's fewest-switches surface hopping approach to describe nonadiabatic electron–ion dynamics. To enable large NAQMD simulations, a series of techniques are employed for efficiently calculating long-range exact exchange correction and excited-state forces. The simulation program is parallelized using hybrid spatial and band decomposition, and is tested for various materials.

© 2012 Elsevier B.V. All rights reserved.

1. Introduction

Molecular dynamics involving electronic transitions is important in various processes such as photoexcitation dynamics of electrons and ions [1]. In nonadiabatic quantum molecular dynamics (NAQMD) simulation [2–8] based on the fewest-switches surface-hopping (FSSH) approach [9,10], electrons at each time instance occupy one of the excited eigenstates corresponding to the atomic configuration at the same time instance, and transitions between the excited states are made stochastically according to the transition probability determined by non-adiabatic coupling (NAC). The NAC between excited states is described by a density matrix, and its time evolution is calculated using time-dependent density functional theory (TDDFT) [11–16]. Here, ionic motions follow the classical Newtonian mechanics, where interatomic forces are computed quantum mechanically based on the Hellmann–Feynman theorem [1].

In order to include many-body effects in NAQMD, electronic excited states are described as a linear combination of electron–hole

pairs within the linear-response TDDFT (LR-TDDFT) [4,5,17–19]. In LR-TDDFT, electronic excitation energies are calculated from the poles of an electron–hole pair response function. This amounts to solving an eigenvalue problem, where many-body effects are introduced through coupling matrix elements consisting of the random-phase-approximation (RPA) and exchange–correlation (xc) terms, with the latter represented by the xc functional. Retaining only the RPA term amounts to summing ring diagrams in perturbative expansion of the response function, which accounts for collective electron dynamics such as plasmons [20]. Static local xc functionals such as the generalized gradient approximation (GGA) [21] do not change the situation drastically. TDDFT simulations with local xc functionals have been used to study dynamic correlation effects such as plasmon-assisted resonant tunneling [22,23].

In LR-TDDFT, electronic excited states are often expanded in terms of ground-state Kohn–Sham (KS) orbitals [24] in density functional theory (DFT) [25,26] as a basis set. Using a local xc functional such as GGA in this procedure leads to several known problems. First, electronic band gaps of semiconductors and insulators are underestimated. This problem may be rectified by introducing the self-energy within the GW approximation [27], or through self-interaction correction (SIC) [28] within DFT. TDDFT simulations with SIC [29] have accurately reproduced exact current–voltage characteristics of quantum dot diodes [30].

* Corresponding author at: Collaboratory for Advanced Computing and Simulations, Department of Physics & Astronomy, University of Southern California, Los Angeles, CA 90089-0242, USA.

E-mail address: anakano@usc.edu (A. Nakano).

The second problem is that any local xc functional fails to describe a charge-transfer (CT) excited state at large molecular separation, e.g., in a dimer of electron donor and acceptor molecules in vacuum [31]. Here, the correct long-range CT is described by the nonlocal Hartree–Fock (HF) exchange potential [31]. This is understandable, since the binding of an electron–hole pair (or exciton) is described by summing ladder diagrams in perturbative expansion, instead of the ring diagrams in RPA, and the two types of diagrams are interrelated through the exchange operation, i.e. swapping the labels of electronic orbitals [20]. This problem can be remedied by many-body approaches such as the Bethe–Salpeter equation (BSE) [32], or within LR-TDDFT using range-separated hybrid xc functionals that incorporate long-range exact exchange correction [33,34].

Though the generalized KS scheme [24,35] based on hybrid exact-exchange functionals thus resolves the known deficiency of LR-TDDFT using local GGA-type KS schemes, it incurs orders-of-magnitude larger computational costs due to the required exchange integrals between electronic-orbital pairs. Recently, a number of approaches have been proposed to speed up this computation, including a compact representation of the exchange operator [36] and hardware acceleration of exchange integrals using graphics processing units [37]. However, NAQMD simulation using hybrid functionals and large basis sets (e.g. the plane-wave basis set) remains a challenge for systems involving over 100 atoms. This is a serious drawback, since many applications (e.g. molecular design of electron donor/acceptor interfaces for efficient solar cells) require many hundreds of atoms to represent molecular orientations and interfacial morphologies [38]. Here, such large NAQMD simulations are enabled by employing a recently proposed non-self-consistent (NSC) approximation [39] to hybrid functionals.

Another major computational cost in the LR-TDDFT based NAQMD simulation is associated with the calculation of interatomic forces, when the electrons are in an excited state. Various computational approaches have been proposed to speed up excited-state force calculations [40,41], but those for NAQMD simulations involving hundreds of atoms are still prohibitive. Here, we adopt a NSC excited-state force calculation method based on a modified Harris–Foulkes approach [42–44], which achieves an asymptotic $O(N)$ speedup compared with the conventional finite-differencing method for an N -electron system while retaining similar accuracy, thereby enabling large NAQMD simulations involving over 500 atoms and many long-time trajectories [7].

We have implemented LR-TDDFT based NAQMD simulations on massively parallel computers using hybrid spatial and band decomposition. To enable large NAQMD simulations using the plane-wave basis set, NSC approximations mentioned above are employed for calculating long-range exact exchange correction and excited-state forces. This paper presents the simulation methods along with its validation for various materials. The rest of the paper is organized as follows. The next section describes the simulation methods. Simulation results are presented in Section 3, while Section 4 contains a summary.

2. Simulation methods

2.1. Electronic ground states

As a basis set for representing electronic excited states in LR-TDDFT, we use ground-state KS orbitals [24] within DFT [25,26]. To do so, we first obtain adiabatic electronic ground states using the projector-augmented-wave method [45,46], which is an all-electron electronic-structure-calculation method within the frozen-core approximation in the framework of DFT. The GGA [21] is used for the xc energy with nonlinear core corrections [47].

The electronic pseudo-wave functions and the pseudo-charge density are expanded by plane waves. The energy functional is minimized with respect to KS orbitals by an iterative method [48,49].

In DFT, the total energy E_{KS} of an N -electron system is written in atomic units as

$$E_{KS} = \sum_s f_s \langle \psi_s | \left(-\frac{1}{2} \nabla^2 + \hat{V}_{ion} \right) | \psi_s \rangle + \frac{1}{2} \iint d\mathbf{r} d\mathbf{r}' \frac{\rho(\mathbf{r})\rho(\mathbf{r}')}{|\mathbf{r} - \mathbf{r}'|} + E_{xc}[\rho], \quad (1)$$

where ψ_s and f_s are the s -th one-electron KS orbital and its occupation number, respectively, ∇^2 is the Laplacian operator, \hat{V}_{ion} is the electron–ion potential, and the electron density $\rho(\mathbf{r})$ is given by

$$\rho(\mathbf{r}) = \sum_s f_s |\psi_s(\mathbf{r})|^2. \quad (2)$$

The second and third terms in the right-hand side of Eq. (1) are the Hartree energy and the xc energy functional, respectively.

Minimization of E_{KS} with respect to a set of KS orbitals, $\{\psi_s\}$, under orthonormalization constraints,

$$\langle \psi_s | \psi_t \rangle = \delta_{s,t}, \quad (3)$$

leads to the KS equations:

$$\hat{H}_{KS} |\psi_s\rangle \equiv \left(-\frac{1}{2} \nabla^2 + \hat{V}_{ion} + \hat{V}_H + \hat{V}_{xc} \right) |\psi_s\rangle = \varepsilon_s |\psi_s\rangle, \quad (4)$$

where ε_s is the KS eigenvalue for the s -th orbital. The Hartree potential \hat{V}_H and the xc potential \hat{V}_{xc} , respectively, are given by

$$\hat{V}_H(\mathbf{r}) = \int d\mathbf{r}' \frac{\rho(\mathbf{r}')}{|\mathbf{r} - \mathbf{r}'|}, \quad (5)$$

$$\hat{V}_{xc}(\mathbf{r}) = \frac{\delta E_{xc}}{\delta \rho(\mathbf{r})}. \quad (6)$$

The electronic ground state is determined self-consistently, i.e., the electron density is obtained iteratively until the input density $\rho_{in}(\mathbf{r})$, which is used to calculate the electronic potential, $\hat{V}^{in} = \hat{V}_{ion} + \hat{V}_H^{in} + \hat{V}_{xc}^{in}$, becomes equal to the output density $\rho_{out}(\mathbf{r})$ calculated from Eq. (2) using the KS orbitals, $\{\psi_s(\mathbf{r})\}$, obtained by solving the KS equations, Eq. (4).

Next, we include the long-range exchange correction (LC) through a range-separated hybrid exact exchange functional [34], starting from the self-consistent GGA KS orbitals explained above. In a range-separated functional, the Coulomb-repulsion operator $1/r_{12}$ is divided into short-range and long-range parts using the error function:

$$\frac{1}{r_{12}} = \frac{1 - \text{erf}(\mu r_{12})}{r_{12}} + \frac{\text{erf}(\mu r_{12})}{r_{12}}, \quad (7)$$

where $r_{12} = |\mathbf{r}_1 - \mathbf{r}_2|$ is the distance between two electrons at \mathbf{r}_1 and \mathbf{r}_2 , and μ is a range-separation parameter. The range-separated xc energy functional is then given by

$$E'_{xc} = E_{c,GGA} + E_{x,GGA}^{SR} + E_{x,HF}^{LR}, \quad (8)$$

where $E_{c,GGA}$ is the GGA correlation energy functional, $E_{x,GGA}^{SR}$ is the short-range part of the GGA exchange energy functional, and $E_{x,HF}^{LR}$ is the long-range part of the HF exchange integral (i.e., using the second term in Eq. (7) as the Coulomb-repulsion operator).

In the NSC approximation by Zhang et al. [39], long-range corrected Hamiltonian matrix elements are constructed from the self-consistent GGA KS orbitals as

$$H'_{st} = \delta_{st} \varepsilon_t - \langle \psi_s | V_{x,GGA}^{LR}[\rho(\mathbf{r})] | \psi_t \rangle - \sum_{i \in \{\text{occupied}\}} [\psi_s^* \psi_i | \text{erf}(\mu r) / r | \psi_i^* \psi_t], \quad (9)$$

where $V_{x,GGA}^{LR}(\mathbf{r}) = \delta E_{x,GGA}^{LR} / \delta \rho(\mathbf{r})$, with $E_{x,GGA}^{LR}$ the long-range part of the GGA exchange energy functional, and the Coulomb-like integral is defined as

$$[f|h(r)|g] \equiv \iint d\mathbf{r}d\mathbf{r}' f(\mathbf{r})h(|\mathbf{r}-\mathbf{r}'|)g(\mathbf{r}'). \quad (10)$$

We diagonalize the Hamiltonian matrix, Eq. (9), as

$$\sum_t H'_{st} U_{tu} = U_{su} \epsilon'_u, \quad (11)$$

to obtain long-range corrected KS (LC-KS) energies ϵ'_s and orbitals,

$$\psi'_s(\mathbf{r}) = \sum_t \psi_t(\mathbf{r}) U_{ts}. \quad (12)$$

In the NSC approximation, the compute-intensive exchange integrals in the last term of Eq. (9) are computed only once, thereby significantly reducing the excessive computational cost of the self-consistent range-separated hybrid exact exchange scheme. Here, the long-range interaction is computed using the reciprocal-space formalism of Martyna and Tuckerman [50] to avoid the interaction with electrons in the periodically-repeated image cells.

2.2. Electronic excitations

We describe electronic excited states as a linear combination of electron-hole pairs within Casida's LR-TDDFT [4,5,17–19], using the ground-state LC-KS orbitals as a basis set. In LR-TDDFT, electronic excitation energies are calculated from the poles of an electron-hole pair response function. This amounts to solving a non-Hermitian eigenvalue problem [17],

$$\begin{pmatrix} \mathbf{A} & \mathbf{B} \\ \mathbf{B}^* & \mathbf{A}^* \end{pmatrix} \begin{pmatrix} \mathbf{X}_I \\ \mathbf{Y}_I \end{pmatrix} = \omega_I \begin{pmatrix} \mathbf{1} & \mathbf{0} \\ \mathbf{0} & -\mathbf{1} \end{pmatrix} \begin{pmatrix} \mathbf{X}_I \\ \mathbf{Y}_I \end{pmatrix}, \quad (13)$$

where the eigenvalue ω_I is the I -th excitation energy, with the corresponding eigenvectors \mathbf{X}_I and \mathbf{Y}_I . In Eq. (13), the elements of the \mathbf{A} and \mathbf{B} matrices are given by

$$A_{ai\sigma,bj\tau} = \delta_{a,b} \delta_{i,j} \delta_{\sigma,\tau} (\epsilon'_{a\sigma} - \epsilon'_{i\sigma}) + K_{ai\sigma,bj\tau}, \quad (14)$$

$$B_{ai\sigma,bj\tau} = K_{ai\sigma,jb\tau}, \quad (15)$$

where the indices i, j and a, b are used for occupied and virtual orbitals, respectively, σ, τ are spin variables, and $\epsilon'_{i\sigma}$ is the i -th LC-KS orbital energy with spin σ . For a range-separated xc functional [33,34], the coupling matrix elements in Eqs. (14) and (15) are given by

$$\begin{aligned} K_{ai\sigma,bj\tau} &= [\psi'_{a\sigma} \psi'_{i\sigma} | 1/r | \psi'_{j\tau} \psi'_{b\tau}] \\ &\quad - \delta_{\sigma,\tau} [\psi'_{a\sigma} \psi'_{b\tau} | \text{erf}(\mu r) / r | \psi'_{j\tau} \psi'_{i\sigma}] \\ &\quad + \int d\mathbf{r} \int d\mathbf{r}' \psi'_{a\sigma}(\mathbf{r}) \psi'_{i\sigma}(\mathbf{r}') \\ &\quad \times \frac{\delta^2 (E_{xc,GGA} - E_{xc,GGA}^{LR})}{\delta \rho_\sigma(\mathbf{r}) \delta \rho_\tau(\mathbf{r}')} \psi'_{j\tau}(\mathbf{r}) \psi'_{b\tau}(\mathbf{r}'), \end{aligned} \quad (16)$$

where $E_{xc,GGA}$ is the xc functional within GGA and $\rho_\sigma(\mathbf{r})$ is the electron density with spin σ . The size of the \mathbf{A} , \mathbf{B} and \mathbf{K} matrices in Eqs. (14)–(16) is $N_o N_u \times N_o N_u$, where N_o and N_u respectively are the numbers of occupied and unoccupied LC-KS orbitals used to represent excited states.

According to the assignment ansatz by Casida [17], the many-body wave function of the I -th excited state is given by [39,51]

$$|\Phi_I\rangle = \sum_{i \in \{\text{occupied}\}} \sum_{a \in \{\text{unoccupied}\}} \sum_{\sigma} \frac{X_{I,ai\sigma} + Y_{I,ai\sigma}}{\sqrt{\omega_I}} \hat{c}_{a\sigma}^+ \hat{c}_{i\sigma} |\Phi_0\rangle, \quad (17)$$

where $|\Phi_0\rangle$ is the Slater determinant of the occupied LC-KS orbitals, and $\hat{c}_{s\sigma}^+$ and $\hat{c}_{s\sigma}$ are the creation and annihilation operators acting on the s -th LC-KS orbital of spin σ .

2.3. Molecular dynamics

Molecular dynamics (MD) simulations are carried out in the canonical ensemble using the Nosé–Hoover thermostat technique [52,53]. The equations of motion are integrated numerically using an explicit reversible integrator [54]. In the MD simulations, interatomic forces are computed quantum mechanically based on the Hellmann–Feynman theorem [1]. For an excited electronic state, we use a NSC method to evaluate accurate forces at a moderate computational cost. This method is an extension of the Harris–Foulkes approach adopted by Ref. [44] in a different context.

Here, the NSC Harris–Foulkes energy E_{NSC} is defined as [42–44]

$$E_{NSC} = \sum_s f_s \frac{\langle \psi_s | \hat{H}_{KS} | \psi_s \rangle}{\langle \psi_s | \psi_s \rangle} - E_{dc}, \quad (18)$$

where E_{dc} represents double-counting terms related to the Hartree and xc energies:

$$E_{dc} = -\frac{1}{2} \int d\mathbf{r} \rho(\mathbf{r}) V_H(\mathbf{r}) + E_{xc}[\rho] - \int d\mathbf{r} \rho(\mathbf{r}) V_{xc}(\mathbf{r}). \quad (19)$$

When the electron density achieves self-consistency, E_{NSC} coincides with the KS energy E_{KS} . In practical calculations, the self-consistency is judged whether the difference between $\rho_{in}(\mathbf{r})$ and $\rho_{out}(\mathbf{r})$ is within a given tolerance. Even when the self-consistency is not satisfied, E_{NSC} deviates from the self-consistent energy only by an amount of second order in the deviation of $\rho_{in}(\mathbf{r})$ from the self-consistent density $\rho(\mathbf{r})$, while E_{KS} deviates by an amount of first order.

The force \mathbf{F}_k acting on the k -th atom is derived from E_{NSC} in Eq. (18) as

$$\begin{aligned} \mathbf{F}_k &= -\frac{\partial}{\partial \mathbf{R}_k} \left(E_{NSC} + \sum_{l < m} \frac{z_l z_m}{|\mathbf{R}_l - \mathbf{R}_m|} \right) \\ &= \mathbf{F}_k^{\text{Hellmann-Feynman}} + \mathbf{F}_k^{\text{NSC}}, \end{aligned} \quad (20)$$

where \mathbf{R}_k and z_k are the position and the valence, respectively, of the k -th atom. In Eq. (20), the NSC force $\mathbf{F}_k^{\text{NSC}}$ is given by

$$\begin{aligned} \mathbf{F}_k^{\text{NSC}} &= \iint d\mathbf{r}d\mathbf{r}' \frac{\delta \rho(\mathbf{r}')}{|\mathbf{r} - \mathbf{r}'|} \left\{ -\frac{\partial}{\partial \mathbf{R}_k} \rho_{in}(\mathbf{r}) \right\} \\ &\quad + \int d\mathbf{r} \delta \rho(\mathbf{r}) \left\{ -\frac{\partial}{\partial \mathbf{R}_k} V_{xc}(\mathbf{r}) \right\}, \end{aligned} \quad (21)$$

where $\delta \rho(\mathbf{r}) = \rho_{out}(\mathbf{r}) - \rho_{in}(\mathbf{r})$. If the electron density is obtained self-consistently, there is no contribution from $\mathbf{F}_k^{\text{NSC}}$ since $\delta \rho(\mathbf{r}) = 0$.

Let us rewrite the I -th excited state Φ_I , Eq. (17), in the LR-TDDFT method [4,5,17–19] as

$$\Phi_I = \sum_{ia\sigma} C_{I,ai\sigma} \hat{c}_{a\sigma}^+ \hat{c}_{i\sigma} \Phi_0 \equiv \sum_{ia\sigma} C_{I,ai\sigma} \Phi_{ai\sigma}, \quad (22)$$

where $\Phi_{ai\sigma}$ is the Slater determinant obtained by replacing the i -th orbital by the a -th orbital in Φ_0 . The excitation energy ω_I is formally written as

$$\omega_I = \langle \Phi_I | \hat{H}_N | \Phi_I \rangle, \quad (23)$$

where \hat{H}_N is the Hamiltonian of the N -electron system. Atomic forces in the excited state are usually calculated by finite differencing, in which atoms are slightly displaced and forces are calculated from the corresponding energy difference. For a system consisting of N_{atom} atoms, this finite-difference approach requires $3N_{\text{atom}}$ self-consistent calculations to account for displacements along the three Cartesian directions of all atoms. This prohibitive

computational cost has thus far precluded LR-TDDFT based NAQMD simulations involving hundreds of atoms.

To reduce the computational cost of calculating excited-state forces, we first employ a diagonal approximation defined as

$$\begin{aligned} \mathbf{F}_k &= -\frac{\partial}{\partial \mathbf{R}_k} \left(\omega_l + \sum_{l < m} \frac{z_l z_m}{|\mathbf{R}_l - \mathbf{R}_m|} \right) \\ &\sim -\frac{\partial}{\partial \mathbf{R}_k} \left(\sum_{i\alpha\sigma} |C_{l,i\alpha\sigma}|^2 \langle \Phi_{i\alpha\sigma} | \hat{H}_N | \Phi_{i\alpha\sigma} \rangle \right. \\ &\quad \left. + \sum_{l < m} \frac{z_l z_m}{|\mathbf{R}_l - \mathbf{R}_m|} \right). \end{aligned} \quad (24)$$

In the spirit of the NSC force, we evaluate the first term of Eq. (24) using the LC-KS orbitals ψ'_s and their occupation numbers $f_s^{i\alpha\sigma}$ in $\Phi_{i\alpha\sigma}$ as

$$\begin{aligned} &-\frac{\partial}{\partial \mathbf{R}_k} \langle \Phi_{i\alpha\sigma} | \hat{H}_N | \Phi_{i\alpha\sigma} \rangle \\ &= -\frac{\partial}{\partial \mathbf{R}_k} \left\{ \sum_s f_s^{i\alpha\sigma} \frac{\langle \psi'_s | \hat{H}_{KS} | \psi'_s \rangle}{\langle \psi'_s | \psi'_s \rangle} - E_{dc} \right\} \\ &= F_k^{\text{Hellmann-Feynman}} + F_k^{\text{NSC},i\alpha\sigma}. \end{aligned} \quad (25)$$

Here, we have used

$$\rho'_{i\alpha\sigma}(\mathbf{r}) = \sum_s f_s^{i\alpha\sigma} |\psi'_s(\mathbf{r})|^2 \quad (26)$$

as $\rho_{\text{out}}(\mathbf{r})$, and the ground-state electron density as $\rho_{\text{in}}(\mathbf{r})$ to evaluate $\mathbf{F}_k^{\text{NSC},i\alpha\sigma}$.

In addition to the use of $\rho'_{i\alpha\sigma}(\mathbf{r})$ as $\rho_{\text{out}}(\mathbf{r})$ in the NSC excited-force calculation, we propose a modified approach based on a mixing scheme for the electron density, which often improves the convergence of self-consistent iterations in electronic-structure calculations. Here, we employ a mixing scheme for Fourier components $\rho(\mathbf{G})$ of $\rho(\mathbf{r})$ proposed by Kerker [55]:

$$\tilde{\rho}'_{i\alpha\sigma}(\mathbf{G}) = \rho_{\text{in}}(\mathbf{G}) + \frac{A\mathbf{G}^2}{\mathbf{G}^2 + B} [\rho'_{i\alpha\sigma}(\mathbf{G}) - \rho_{\text{in}}(\mathbf{G})], \quad (27)$$

where A and B are parameters to be optimized. Our NSC excited-force calculation based on a modified Harris–Foulkes approach uses Eqs. (24) and (25), where $\tilde{\rho}'_{i\alpha\sigma}(\mathbf{G})$ in Eq. (27) is used as ρ_{out} , along with the electron density of the ground state as $\rho_{\text{in}}(\mathbf{r})$, to evaluate the value of $\mathbf{F}_k^{\text{NSC},i\alpha\sigma}$ using Eq. (21).

A recent paper has pointed out a problem associated with the excited-state force calculation based on the Casida ansatz in Eq. (17) [41]. Namely, certain symmetric properties are not preserved in the calculated forces. For example, Haruyama et al. have reported a violation of Newton's third law for the excited-state forces in a heteronuclear diatomic molecule calculated using the many-body wave function based on the Casida ansatz [41]. To rectify this problem for a crystalline material, the forces have to be corrected to satisfy the crystal symmetries. For a disordered material or a heteronuclear diatomic molecule, at least the following correction must be made:

$$\mathbf{F}_k^c = \mathbf{F}_k - \bar{\mathbf{F}} = \mathbf{F}_k - \frac{1}{N_{\text{atom}}} \sum_{k=1}^{N_{\text{atom}}} \mathbf{F}_k, \quad (28)$$

so as to conserve the total momentum. To conserve the total angular momentum, the torque must be made zero as well.

2.4. Nonadiabatic electron–ion dynamics

In NAQMD simulations with electronic transitions using Tully's FSSH method [9,10] along with the LC-KS representation of TDDFT,

we calculate the time evolution of the density matrix with a fixed atomic configuration between consecutive MD steps. The elements of the density matrix determine the switching probability between the adiabatic states. These equations are derived by expanding the electronic state $\Psi(t)$ at time t in terms of the electronic excited states $\Phi_j(\mathbf{R}(t))$ in LR-TDDFT corresponding to the atomic configuration $\mathbf{R}(t)$ at time t :

$$|\Psi(t)\rangle = \sum_j C_j^{(l)}(t) |\Phi_j(\mathbf{R}(t))\rangle, \quad C_j^{(l)}(0) = \delta_{l,j}. \quad (29)$$

The time evolution of the expansion coefficients $C_j^{(l)}(t)$ is governed by

$$\frac{d}{dt} C_j^{(l)}(t) = -\sum_k (i\omega_k \delta_{jk} + D_{jk}) C_k^{(l)}(t), \quad (30)$$

where the NAC elements are defined as [4,5]

$$D_{jk} = \langle \Phi_j | \frac{\partial}{\partial t} | \Phi_k \rangle. \quad (31)$$

The NAC elements are calculated from a pair of excited-state wave functions at consecutive time steps in an adiabatic QMD simulation by finite differencing. The use of the many-body wave function, Eq. (17), in Eq. (31) has been shown to be exact between ground and singly excited states, as well as between any pair of excited states when the Tamm–Dancoff approximation is used [51]. Various approaches have been proposed to improve FSSH for describing coupled electron–ion dynamics involving nonadiabatic electronic processes [56–58]. These approaches incorporate, e.g., quantum uncertainty [58] for better accuracy, and are recommended when implementing new NAQMD codes.

2.5. Parallel implementation

The NAQMD simulation has been implemented on massively parallel computers [49] by a hybrid approach combining band decomposition (i.e., assigning the calculations of different KS orbitals to different processors) and spatial decomposition (i.e., distributing real-space or reciprocal-space grid points among processors). The iterative band-by-band minimization is carried out by the band decomposition, where the eigenenergy of each band is minimized in each processor independently from the others under an approximate orthonormal condition. The electron density is also calculated by the band decomposition. On the other hand, the Gram–Schmidt orthonormalization of the KS orbitals is executed in the reciprocal-space decomposition scheme, where the Fourier components of the wave functions are distributed among multiple processors. To switch between these two schemes, all-to-all communications are required. In addition, global communication is necessary to calculate the scalar products between the wave functions. The program is implemented using the message passing interface (MPI) library [59] for interprocessor communications.

3. Simulation results

3.1. Energy-band alignment

The NSC approach to range-separated hybrid exact-exchange functionals has been validated for various molecules including N_2 , CO , C_6H_6 , and H_2CO [39]. To test the approach for a larger system, we calculate the alignment of electronic energy levels for a quaterthiophene (QT) molecule ($\text{CH}_3-(\text{C}_{14}\text{H}_{16}\text{S}_2)_2-\text{CH}_3$) on a zinc-oxide (ZnO) (10 $\bar{1}0$) surface (containing 240 Zn and 240 O atoms), where the total QT/ZnO system contains 552 atoms (see the inset in Fig. 1). Periodic boundary conditions are applied to all Cartesian

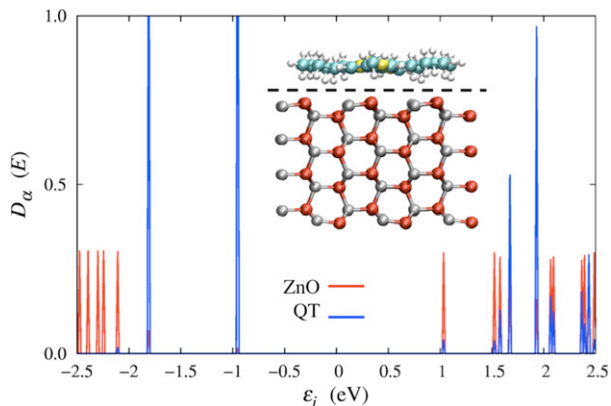


Fig. 1. Electronic densities of states $D_\alpha(E)$ for the ground state of the QT/ZnO system, where the red and blue curves are for $\alpha = \text{ZnO}$ and QT, respectively. The inset shows the simulated system, where the red, gray, cyan, yellow and white spheres represent O, Zn, C, S and H atoms, respectively. The dashed line in the inset defines the boundary between the QT and ZnO spatial regions.

directions for the simulation supercell of dimensions $28.07 \times 15.56 \times 21 \text{ \AA}^3$. The electronic pseudo-wave functions and the pseudo-charge density are expanded by plane waves with cutoff energies of 30 and 250 Ry, respectively. This material combination is used in hybrid organic/inorganic solar cells, for which their band alignment is essential [60].

The energy levels for the minimum-energy atomic configuration are shown in Fig. 1, which shows partial electronic densities of states (DOS) $D_\alpha(E)$ projected onto the wave functions of the atoms in the α -th molecular subsystems ($\alpha = \text{ZnO}$ or QT), where the energy is measured relative to the Fermi energy. The highest occupied molecular orbital (HOMO) at -0.95 eV spreads only within QT, reflected in a peak of $D_{QT}(E)$, and its wave function is nearly identical to the HOMO of isolated QT [7]. On the other hand, the lowest unoccupied molecular orbital (LUMO) at 1.04 eV resides only within ZnO, and the corresponding peak is in $D_{\text{ZnO}}(E)$. The lowest unoccupied orbitals with the largest wave-function amplitudes within QT is LUMO + 4 (1.93 eV), which thus represents the LUMO of QT or LUMO(QT). Here, we denote the m -th lowest unoccupied orbital but one as LUMO + m . The highest occupied molecular orbital but two (i.e., HOMO - 2) at -2.11 eV is a ZnO state with no mixture of QT orbitals. We therefore call HOMO - 2 to be the HOMO of ZnO or HOMO(ZnO). The calculation correctly describes the known staggered band alignment between QT and ZnO. The calculated energy gap between HOMO(QT) and LUMO(QT) is 2.88 eV , which agrees reasonably with the observed value of 3.16 eV for QT [61]. Also, the calculated energy gap between HOMO(ZnO) and LUMO(ZnO) is 3.15 eV , which also agrees reasonably with the experimental value of 3.4 eV [62].

3.2. Charge-transfer excitation energy

The CT excitation energy calculated using the NSC approach to range-separated hybrid exact-exchange functionals has been validated for a $\text{C}_2\text{H}_4\text{-C}_2\text{F}_4$ dimer [39]. Here, we estimate the effect of different xc functionals in describing CT excited states between rubrene and C_{60} molecules [8]. The simulation supercell size is $18 \times 18 \times 24 \text{ \AA}^3$ with periodic boundary conditions in all directions, where the electronic pseudo-wave functions and the pseudo-charge density are expanded by plane waves with cutoff energies of 30 and 250 Ry, respectively.

Fig. 2 plots the CT excitation energy calculated by Casida's LR-TDDFT as a function of the distance r between rubrene and C_{60} molecules [8]. (Here, $r = 0$ signifies the distance for the minimum-energy configuration.) The diamond and square symbols respectively show the excitation energies with and without the

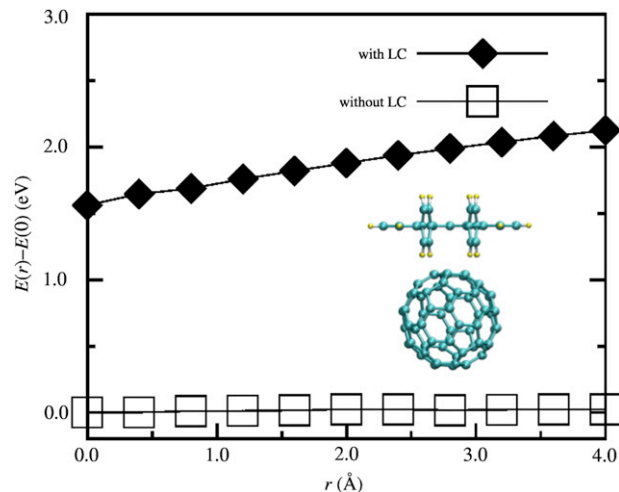


Fig. 2. Charge-transfer excitation energy as a function of the rubrene- C_{60} distance. The diamond and square symbols indicate the excitation energies with and without long-range exact exchange correction (LC), respectively. (Here, the energy is measured relative to that without LC at $r = 0$.) The inset shows the simulated rubrene and C_{60} molecules, where the cyan and yellow spheres represent C and H atoms, respectively.

long-range exact exchange correction (LC) described in Section 2.1. The result with LC exhibits the correct asymptotic $-1/r$ behavior [31]. Describing CT excited states correctly at an interface between an electron donor, rubrene, and a C_{60} acceptor is essential for molecular design of interfacial structures for efficient organic solar cells composed of these materials [38].

3.3. Excited-state forces

We validate the excited-state NSC force \mathbf{F}_k in Eqs. (24) and (25) for a S_8 molecule, which forms a crown-shaped ring [63]. An fcc supercell of lattice constant 18 \AA is used. The plane-wave cutoff energies are 20 and 120 Ry for the electronic pseudo-wave functions and the pseudo-charge density, respectively. For the lowest triplet excited state, a self-consistent solution is easily obtained, since it is the “ground state” of that spin configuration, while it is computationally highly demanding to obtain it for other excited states. For comparison between the excited-state NSC forces \mathbf{F}_k with the forces $\mathbf{F}_k^{\text{SCF}}$ obtained self-consistently, we define a quantity,

$$\Delta = 1 - \left\langle \frac{\mathbf{F}_k \bullet \mathbf{F}_k^{\text{SCF}}}{\mathbf{F}_k^{\text{SCF}} \bullet \mathbf{F}_k^{\text{SCF}}} \right\rangle, \quad (32)$$

where the bracket denotes the average over all atoms, and Δ becomes zero if \mathbf{F}_k is equal to $\mathbf{F}_k^{\text{SCF}}$ for all atoms k . Taking an atomic configuration from a trajectory obtained by an adiabatic MD simulation at 300 K, we calculate the energy and forces for the lowest triplet excited state self-consistently. We obtain $\Delta = -0.3 \pm 0.2$ if the forces in the ground state are used as \mathbf{F}_k . When the excited-state forces are calculated by Eqs. (24) and (25) using $\rho'_{\text{ais}}(\mathbf{r})$ as $\rho_{\text{out}}(\mathbf{r})$, a larger value of $\Delta = 0.85 \pm 0.4$ is obtained. With our modified Harris-Foulkes approach, the Δ value is reduced significantly: The smallest value of $\Delta = 0.005 \pm 0.08$ is obtained when $A = 0.9$ and $B = 0.6$ (bohr^{-2}) are used in Eq. (27).

To investigate time-dependent properties of the excited state, we carry out a MD simulation using the self-consistent excited-state forces. Time evolution of the self-consistent excitation energy is shown by the solid line in Fig. 3. One of the S-S bonds

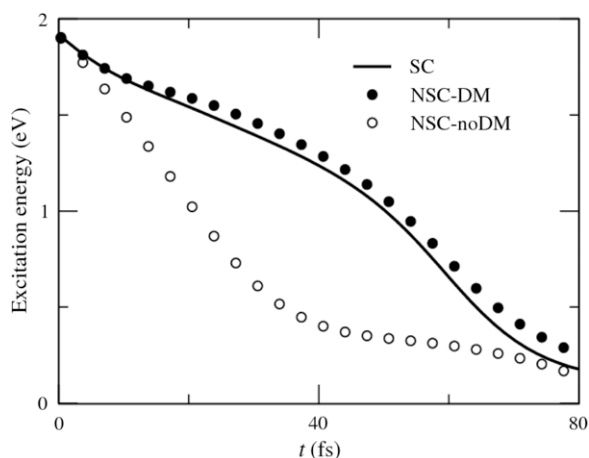


Fig. 3. Time evolution of the excitation energy of the lowest triplet state of a S_8 molecule. The solid line indicates the results using the self-consistent forces (SC). The solid and open circles show the results using the NSC atomic forces obtained by Eqs. (24) and (25) with and without the density mixing (DM) of Eq. (27) (NSC-DM and NSC-noDM), respectively.

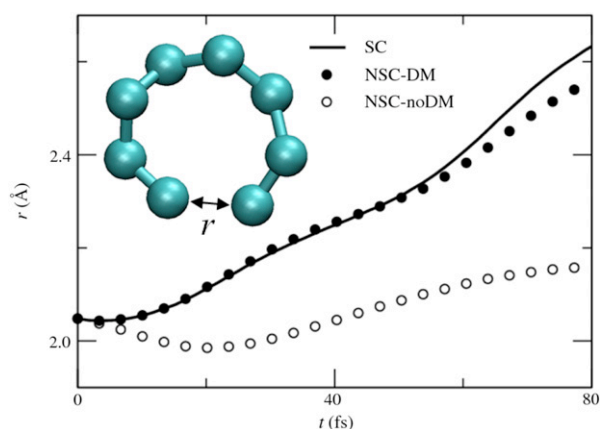


Fig. 4. Time evolution of the bond length in the lowest triplet state of a S_8 molecule. The solid line indicates the results using the self-consistent forces (SC). The solid and open circles show the results using the NSC atomic forces obtained by Eqs. (22) and (23) with and without the density mixing (DM) of Eq. (25) (NSC-DM and NSC-noDM), respectively.

is broken, reflecting the anti-bonding character of the excited state, and the excitation energy decreases, accompanying this structural relaxation. As a comparison, additional MD simulations are performed by using the NSC atomic forces. The solid and open circles show the results using the NSC atomic forces obtained by Eqs. (24) and (25) with and without the density mixing of Eq. (27), respectively. Without density mixing, the excitation energy decreases rapidly with time, which is obviously caused by the fact that the atomic forces between S atoms are incorrect. On the other hand, temporal change of the excitation energy is correctly reproduced by the NSC forces when the density mixing is used.

Fig. 4 shows the time evolution of the length of the S–S bond, which is broken by the excitation. As shown by the open circles, the bond length becomes shorter in the beginning, and elongates eventually, when the density mixing is not used. In this case, the decrease of the excitation energy originates from the shape deformation rather than from the elongation of one of the S–S bonds. With density mixing, the correct structural relaxation is reproduced as shown by the solid circles in Fig. 4. Since the linear-response theory becomes inapplicable in the case of lower

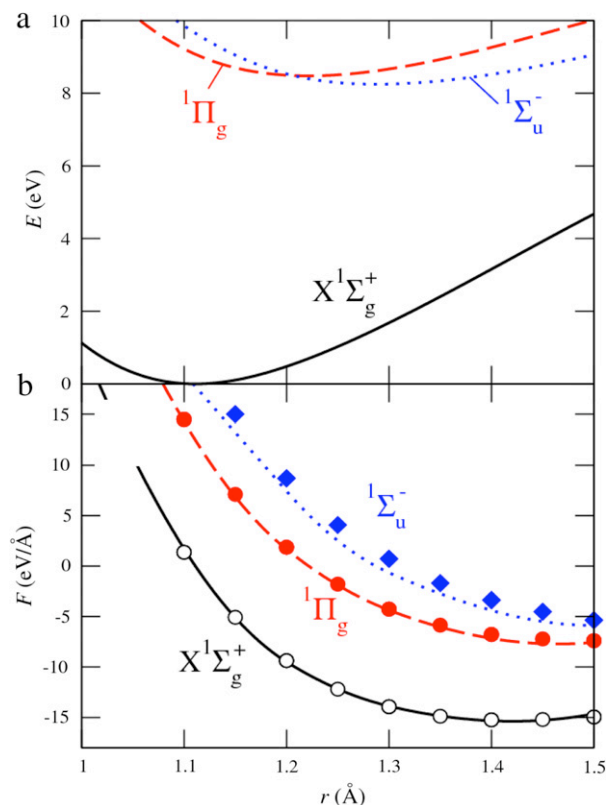


Fig. 5. (a) Adiabatic potential energy $E(r)$ for N_2 molecule as a function of atomic distance r . The solid, dashed and dotted lines correspond to the ground, first-singlet-excited and second-singlet-excited states, respectively. (b) Atomic forces $F(r)$ for N_2 molecule. The solid, dashed and dotted lines show $F(r)$ obtained by the numerical derivatives of $E(r)$ of the ground, first-singlet-excited and second-singlet-excited states, respectively. The open circles show the Hellmann-Feynman forces in the ground state. The solid circles and diamonds show the NSC excited-state forces.

excitation energies, some deviation from the solid line is seen for $t > 60$ fs.

To demonstrate the applicability of the NSC excited-state force calculation to broader materials, we calculate the atomic forces in the excited states of N_2 and CO molecules as in previous studies [40,41]. For these calculations, a cubic supercell of length 12 Å is used. Cutoff energies of 45 and 300 Ry are used to expand the electronic pseudo-wave functions and the pseudo-charge density, respectively. The calculated equilibrium bond lengths are 1.11 and 1.14 Å for N_2 and CO, respectively, which are in good agreement with the respective experimental values, 1.10 and 1.09 Å. The vertical excitation energies from the ground state are also in reasonable agreement with experiments. Note that the numerical values are slightly different from those in Ref. [41], because a different functional is used for the exchange–correlation energy.

Fig. 5(a) shows the adiabatic potential energies of the first- and second-singlet-excited states, $^1\Pi_g$ and $^1\Sigma_u^-$, as well as the ground state, $X^1\Sigma_g^+$, of a N_2 molecule. From the numerical derivatives of these potential-energy surfaces, “true” excited-state forces are obtained as shown by the lines in Fig. 5(b). The NSC excited-state forces are computed using the density mixing with $A = 0.9$ and $B = 0.6$ (bohr $^{-2}$). Although these parameters are not optimized for the N_2 molecule, the results are quite good for the first singlet-excited state (solid circles in Fig. 5(b)). Also, the forces in the second-singlet state are reproduced reasonably well by the NSC calculation (solid diamonds in Fig. 5(b)).

Fig. 6(a) shows the adiabatic potential energies of the ground ($X^1\Sigma^+$) and first-singlet-excited ($A^1\Pi$) states of a CO molecule.

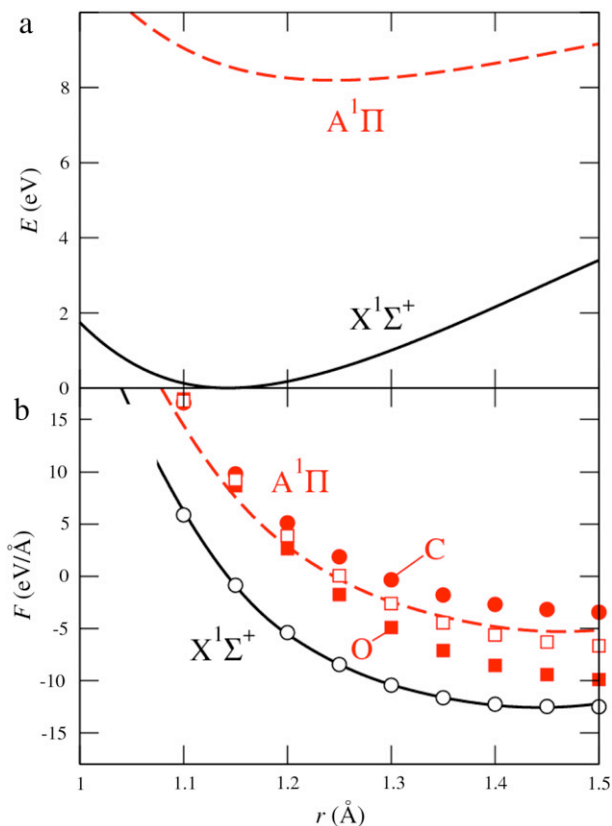


Fig. 6. (a) Adiabatic potential energy $E(r)$ for CO molecule as a function of atomic distance r . The solid and dashed lines correspond to the ground and first-singlet-excited states, respectively. (b) Atomic forces $F(r)$ for CO molecule. The solid and dashed lines show $F(r)$ obtained by the numerical derivatives of $E(r)$ of the ground and first-singlet-excited states, respectively. The open circles show the Hellmann-Feynman forces in the ground state. The solid circles and squares show the NSC excited-state forces acting on C and O atoms, respectively. The direction of the forces on O atom is inverted. The open squares show the corrected excited-state NSC force.

The numerical derivatives of these potential-energy surfaces are shown by the lines in Fig. 6(b). Again, the density mixing with $A = 0.9$ and $B = 0.6$ (bohr^{-2}) is used to calculate the NSC excited-state forces. As shown by the solid squares and circles in Fig. 6(b), the NSC excited-state forces acting on the O and C atoms are different from each other. This is a manifestation of the problem associated with the excited-state force calculation based on the Casida ansatz as discussed in Section 2.3. It should be noted that a more elaborate calculation without the NSC approximation exhibits the same problem [41]. As shown by the open squares and the dashed line in Fig. 6(b), the r dependence of F_k^c with the proposed correction in Eq. (28) is in good agreement with that of the numerical derivatives of the potential-energy surface. The results shown here indicate that our method is practically capable of obtaining the excited-state forces.

Our NAQMD scheme using the excited-state NSC forces involves two main calculations: One is the self-consistent DFT calculation to obtain the ground-state KS orbitals $\{\psi_s\}$, and the other is the LR-TDDFT calculation to obtain the excitation energy ω_l and the coefficients $C_{l,ai\sigma}$. The amount of computation of the former is the same as that in adiabatic QMD simulation. In the latter, most of the computing time is spent for the calculation of the elements of the coupling matrix in the Casida equation. The computational complexity of each element is equivalent to calculating $V_H(\mathbf{r})$ one time plus $V_{xc}(\mathbf{r})$ twice, when the exchange-correlation part is evaluated in a finite-difference scheme [18]. The number of the matrix elements is the square of $2N_{\text{hole}}N_{\text{electron}}$, where N_{hole}

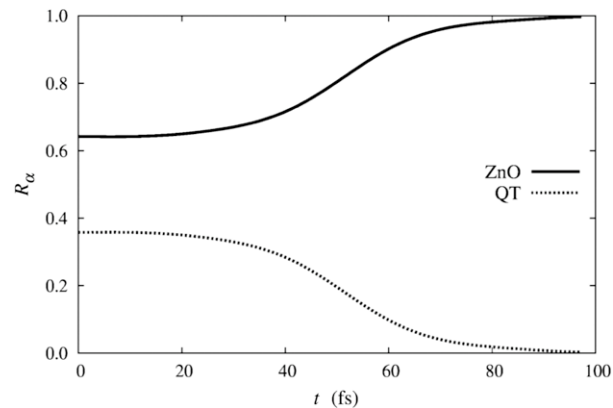


Fig. 7. Averaged time evolution of the existence probabilities $R_\alpha(t)$ of the pseudo-electron in subsystems α . The solid and dotted lines indicate $\alpha = \text{ZnO}$ and QT, respectively.

and N_{electron} are the numbers of hole and electron orbitals to be considered, respectively (the factor 2 comes from spin). In the present calculation for the S_8 molecule, one hole and two electron orbitals are taken into account, and the number of elements becomes 16 ($=4 \times 4$), while the number of the KS orbitals is 40 for each spin. The computing time increases about 30% in the present NAQMD simulation compared with the adiabatic simulations. For larger systems, the number of the elements as well as that of the KS orbitals will become larger. However, the coupling between hole-electron pairs is limited in many cases, and therefore, the number of terms in the sum in Eq. (22) will remain small. If this is the case, calculation for most of the elements can be avoided, and the computing time will be comparable to that of adiabatic MD simulation.

3.4. Charge-transfer rates

As an example of NAQMD simulations, we study photoexcited CT from QT to ZnO at the QT/ZnO interface studied in Section 3.1 (see Fig. 1) [7]. Each NAQMD simulation starts with an electronic excited state that corresponds to the excitation of an electron from HOMO(QT) to LUMO(QT) for a given configuration sampled from adiabatic MD trajectory. In order to estimate the CT rate, we integrate the quasi-electron charge density at the QT side to obtain the probability R_{QT} (i.e., above the dashed line in the inset of Fig. 1, which separates the QT and ZnO spatial regions). Similarly, we calculate R_{ZnO} at the ZnO side (note that $R_{\text{ZnO}} + R_{\text{QT}} = 1$) during the entire electron-transfer process up to ~ 100 fs. Fig. 7 plots an ensemble average over 50 such NAQMD simulations starting from 50 configurations uniformly sampled from an adiabatic MD trajectory. The averaged $R_\alpha(t)$ indicates that rapid CT completes within 70 fs. The corresponding CT rate is 0.014 fs^{-1} .

4. Summary

We have implemented quantum molecular dynamics simulation incorporating nonadiabatic electronic transitions on massively parallel computers to study photoexcitation dynamics of many electrons and ions. The nonadiabatic quantum molecular dynamics simulation is based on Casida's linear response time-dependent density functional theory to describe electronic excited states and Tully's fewest-switches surface hopping approach to describe nonadiabatic electron-ion dynamics. To enable large NAQMD simulations using the plane-wave basis set, NSC approximations have been employed for calculating long-range exact exchange correction and excited-state forces. The simulation

program has been parallelized using hybrid spatial and band decomposition, which has been used for large NAQMD simulations involving over 500 atoms [7].

Acknowledgments

This research was supported by the Department of Energy, Office of Science, Basic Energy Sciences, Materials Science and Engineering Division, Grant # DE-FG02-04ER-46130. The work in Japan was supported by KAKENHI (23104512). Simulations were performed at the University of Southern California using the 20,925-processor Linux cluster at the Center for High Performance Computing and Communications.

References

- [1] D. Marx, J. Hutter, *Ab Initio Molecular Dynamics*, Cambridge University Press, Cambridge, UK, 2009.
- [2] N.L. Doltsinis, D. Marx, *Phys. Rev. Lett.* 88 (2002) 166402.
- [3] W.R. Duncan, C.F. Craig, O.V. Prezhdo, *J. Am. Chem. Soc.* 129 (2007) 8528.
- [4] C.P. Hu, H. Hirai, O. Sugino, *J. Chem. Phys.* 127 (2007) 064103.
- [5] E. Tapavicza, I. Tavernelli, U. Rothlisberger, *Phys. Rev. Lett.* 98 (2007) 023001.
- [6] S. Ohmura, S. Koga, I. Akai, F. Shimojo, R.K. Kalia, A. Nakano, P. Vashishta, *Appl. Phys. Lett.* 98 (2011) 113302.
- [7] W. Mou, S. Ohmura, F. Shimojo, A. Nakano, *Appl. Phys. Lett.* 100 (2012) 203306.
- [8] W. Mou, S. Ohmura, S. Hattori, K. Nomura, F. Shimojo, A. Nakano, *J. Chem. Phys.* 136 (2012) 184705.
- [9] J.C. Tully, *J. Chem. Phys.* 93 (1990) 1061.
- [10] J.R. Schmidt, P.V. Parandekar, J.C. Tully, *J. Chem. Phys.* 129 (2008) 044104.
- [11] E.K.U. Gross, W. Kohn, *Phys. Rev. Lett.* 55 (1985) 2850.
- [12] I. Vasiliev, S. Ogut, J.R. Chelikowsky, *Phys. Rev. Lett.* 82 (1999) 1919.
- [13] C.Y. Yam, S. Yokojima, G.H. Chen, *Phys. Rev. B* 68 (2003) 153105.
- [14] S. Meng, E. Kaxiras, *J. Chem. Phys.* 129 (2008) 054110.
- [15] V. Soto-Verdugo, H. Metiu, E. Gwinn, *J. Chem. Phys.* 132 (2010) 195102.
- [16] M.A.L. Marques, C.A. Ullrich, F. Nogueira, A. Rubio, K. Burke, E.K.U. Gross, *Time-Dependent Density Functional Theory*, Springer-Verlag, Berlin, Germany, 2006.
- [17] M.E. Casida, in: D.P. Chong (Ed.), *Recent Advances in Density Functional Methods (Part I)*, World Scientific, Singapore, 1995, pp. 155–192.
- [18] M. Walter, H. Hakkinen, L. Lehtovaara, M. Puska, J. Enkovaara, C. Rostgaard, J.J. Mortensen, *J. Chem. Phys.* 128 (2008) 244101.
- [19] M.E. Casida, M. Huix-Rotlant, *Annu. Rev. Phys. Chem.* 63 (2012) 287.
- [20] G.D. Mahan, *Many Particle Physics*, Kluwer Academic, New York, NY, 2000.
- [21] J.P. Perdew, K. Burke, M. Ernzerhof, *Phys. Rev. Lett.* 77 (1996) 3865.
- [22] A. Nakano, P. Vashishta, R.K. Kalia, *Phys. Rev. B* 43 (1991) 9066.
- [23] A. Nakano, R.K. Kalia, P. Vashishta, *Appl. Phys. Lett.* 64 (1994) 2569.
- [24] W. Kohn, L.J. Sham, *Phys. Rev.* 140 (1965) A1133.
- [25] P. Hohenberg, W. Kohn, *Phys. Rev.* 136 (1964) B864.
- [26] W. Kohn, P. Vashishta, in: N.H. March, and S. Lundqvist (Eds.), *Theory of the Inhomogeneous Electron Gas*, New York, NY, 1983, pp. 79–147.
- [27] M.S. Hybertsen, S.G. Louie, *Phys. Rev. Lett.* 55 (1985) 1418.
- [28] J.P. Perdew, A. Zunger, *Phys. Rev. B* 23 (1981) 5048.
- [29] D. Hofmann, T. Korzdorfer, S. Kummel, *Phys. Rev. Lett.* 108 (2012) 146401.
- [30] A. Nakano, R.K. Kalia, P. Vashishta, *Phys. Rev. B* 44 (1991) 8121.
- [31] A. Dreuw, M. Head-Gordon, *J. Am. Chem. Soc.* 126 (2004) 4007.
- [32] M. Rohlfing, S.G. Louie, *Phys. Rev. Lett.* 81 (1998) 2312.
- [33] J. Heyd, G.E. Scuseria, M. Ernzerhof, *J. Chem. Phys.* 118 (2003) 8207.
- [34] Y. Tawada, T. Tsuneda, S. Yanagisawa, T. Yanai, K. Hirao, *J. Chem. Phys.* 120 (2004) 8425.
- [35] A. Seidl, A. Gorling, P. Vogl, J.A. Majewski, M. Levy, *Phys. Rev. B* 53 (1996) 3764.
- [36] I. Duchemin, F. Gygi, *Commun. Comput. Phys.* 181 (2010) 855.
- [37] M. Hutchonson, M. Widom, *Commun. Comput. Phys.* 183 (2012) 1422.
- [38] C.W. Schlenker, M.E. Thompson, *Topics in Current Chemistry*, Springer, Berlin, Germany, 2011, pp. 1–38.
- [39] X. Zhang, Z. Li, G. Lu, *J. Phys.: Condens. Matter* 24 (2012) 205801.
- [40] A. Sitt, L. Kronik, S. Ismail-Beigi, J.R. Chelikowsky, *Phys. Rev. A* 76 (2007) 054501.
- [41] J. Haruyama, T. Suzuki, C.P. Hu, K. Watanabe, *Phys. Rev. A* 85 (2012) 012516.
- [42] J. Harris, *Phys. Rev. B* 31 (1985) 1770.
- [43] W.M.C. Foulkes, R. Haydock, *Phys. Rev. B* 39 (1989) 12520.
- [44] A.S. Torralba, D.R. Bowler, T. Miyazaki, M.J. Gillan, *J. Chem. Theory Comput.* 5 (2009) 1499.
- [45] P.E. Blochl, *Phys. Rev. B* 50 (1994) 17953.
- [46] G. Kresse, D. Joubert, *Phys. Rev. B* 59 (1999) 1758.
- [47] S.G. Louie, S. Froyen, M.L. Cohen, *Phys. Rev. B* 26 (1982) 1738.
- [48] G. Kresse, J. Hafner, *Phys. Rev. B* 49 (1994) 14251.
- [49] F. Shimojo, R.K. Kalia, A. Nakano, P. Vashishta, *Commun. Comput. Phys.* 140 (2001) 303.
- [50] G.J. Martyna, M.E. Tuckerman, *J. Chem. Phys.* 110 (1999) 2810.
- [51] I. Tavernelli, B.F.E. Curchod, A. Laktionov, U. Rothlisberger, *J. Chem. Phys.* 133 (2010) 194101.
- [52] S. Nosè, *Mol. Phys.* 52 (1984) 255.
- [53] W.G. Hoover, *Phys. Rev. A* 31 (1985) 1695.
- [54] M. Tuckerman, B.J. Berne, G.J. Martyna, *J. Chem. Phys.* 97 (1992) 1990.
- [55] G.P. Kerker, *Phys. Rev. B* 23 (1981) 3082.
- [56] O.V. Prezhdo, *J. Chem. Phys.* 111 (1999) 8366.
- [57] A.W. Jasper, S. Nangia, C.Y. Zhu, D.G. Truhlar, *Acc. Chem. Res.* 39 (2006) 101.
- [58] A.W. Jasper, S.N. Stechmann, D.G. Truhlar, *J. Chem. Phys.* 116 (2002) 5424.
- [59] W. Gropp, E. Lusk, A. Skjellum, *Using MPI*, MIT Press, Cambridge, MA, 1999.
- [60] A.L. Briseno, T.W. Holcombe, A.I. Boukai, E.C. Garnett, S.W. Shelton, J.J.M. Frechet, P.D. Yang, *Nano Lett.* 10 (2010) 334.
- [61] T. Izumi, S. Kobashi, K. Takimiya, Y. Aso, T. Otsubo, *J. Am. Chem. Soc.* 125 (2003) 5286.
- [62] P. Ravirajan, A.M. Peiro, M.K. Nazeeruddin, M. Graetzel, D.D.C. Bradley, J.R. Durrant, J. Nelson, *J. Phys. Chem. B* 110 (2006) 7635.
- [63] B. Meyer, *Chem. Rev.* 76 (1976) 367.